

Complex dynamic behaviors in hyperbolic-type memristor-based cellular neural network

Ai-Xue Qi(齐爱学), Bin-Da Zhu(朱斌达), and Guang-Yi Wang(王光义)
Citation: Chin. Phys. B, 2022, 31 (**2**): 020502. DOI: 10.1088/1674-1056/ac2b1b
Journal homepage: http://cpb.iphy.ac.cn; http://iopscience.iop.org/cpb

What follows is a list of articles you may be interested in

Energy spreading, equipartition, and chaos in lattices with non-central forces

Arnold Ngapasare, Georgios Theocharis, Olivier Richoux, Vassos Achilleos, and Charalampos Skokos
Chin. Phys. B, 2022, 31 (**2**): 020506. DOI: 10.1088/1674-1056/ac3a5e

Nonlinear dynamics analysis of cluster-shaped conservative flows generated from a generalized thermostatted system

Yue Li(李月), Zengqiang Chen(陈增强), Zenghui Wang(王增会), and Shijian Cang(仓诗建)
Chin. Phys. B, 2022, 31 (**1**): 010501. DOI: 10.1088/1674-1056/ac0a61

Acoustic wireless communication based on parameter modulation and complex Lorenz chaotic systems with complex parameters and parametric attractors

Fang-Fang Zhang(张芳芳), Rui Gao(高瑞), and Jian Liu(刘坚)
Chin. Phys. B, 2021, 30 (**8**): 080503. DOI: 10.1088/1674-1056/ac0905

Control of chaos in Frenkel-Kontorova model using reinforcement learning

You-Ming Lei(雷佑铭) and Yan-Yan Han(韩彦彦)
Chin. Phys. B, 2021, 30 (**5**): 050503. DOI: 10.1088/1674-1056/abd74f

A multi-directional controllable multi-scroll conservative chaos generator: Modelling, analysis, and FPGA implementation

En-Zeng Dong(董恩增), Rong-Hao Li(李荣昊), and Sheng-Zhi Du(杜升之)
Chin. Phys. B, 2021, 30 (**2**): 020505. DOI: 10.1088/1674-1056/abc239

Complex dynamic behaviors in hyperbolic-type memristor-based cellular neural network

Ai-Xue Qi(齐爱学)[1], Bin-Da Zhu(朱斌达)[2], and Guang-Yi Wang(王光义)[2,†]

[1] *Faculty of Aerospace Engineering, Binzhou University, Binzhou* 256603, *China*
[2] *Institute of Modern Circuits and Intelligent Information, Hangzhou Dianzi University, Hangzhou* 310018, *China*

(Received 6 February 2021; revised manuscript received 24 September 2021; accepted manuscript online 29 September 2021)

This paper presents a new hyperbolic-type memristor model, whose frequency-dependent pinched hysteresis loops and equivalent circuit are tested by numerical simulations and analog integrated operational amplifier circuits. Based on the hyperbolic-type memristor model, we design a cellular neural network (CNN) with 3-neurons, whose characteristics are analyzed by bifurcations, basins of attraction, complexity analysis, and circuit simulations. We find that the memristive CNN can exhibit some complex dynamic behaviors, including multi-equilibrium points, state-dependent bifurcations, various coexisting chaotic and periodic attractors, and offset of the positions of attractors. By calculating the complexity of the memristor-based CNN system through the spectral entropy (SE) analysis, it can be seen that the complexity curve is consistent with the Lyapunov exponent spectrum, *i.e.*, when the system is in the chaotic state, its SE complexity is higher, while when the system is in the periodic state, its SE complexity is lower. Finally, the realizability and chaotic characteristics of the memristive CNN system are verified by an analog circuit simulation experiment.

Keywords: memristor, cellular neural network, chaos

PACS: 05.45.Gg, 05.45.Jn, 07.05.Mh **DOI:** 10.1088/1674-1056/ac2b1b

1. Introduction

In 1971, Chua introduced the concept of memristor through using the basic circuit variables charge and magnetic flux.[1] It was not until 2008 that HP Labs proved for the first time the existence of the actual memristive devices with titanium dioxide thin films.[2] The memristor is a nonlinear resistor on a nanometer scale and has non-volatility, and can be used to memorize and store information without using any external power supply. It has important potential applications in nonvolatile memories,[3] nonlinear chaotic circuits, neural network,[4] digital logic circuits, *etc*.

Cellular neural network (CNN) proposed by Chua and Yang is a nonlinear processing unit with locally interconnected, multi-input and single-output.[5,6] The CNN processor to receive and generate analog signals has become a strict structure for complex systems to display their specific behaviors and various forms of computations. In fact, many artificial, physical, chemical, and biological systems can be modeled using the CNN.

In Ref. [7], the properties of the 3-cells CNN attractor were discussed and some new results for the adaptive biological control of the 3-cells CNN attractor were acquired. All the main results are proved by using Lyapunov stability theory. In Ref. [8], an image encryption algorithm based on the six-dimensional chaotic cellular neural network (CNN) was proposed, which is robust to noise/missing pixels in the cryptographic image. In Ref. [9] the implementation of a chaotic CNN-based true random number generator on a field programmable gate array (FPGA) board were presented.

As a fundamental component unit of brain, a neuron is capable of generating intricate dynamical behaviors[10] and the CNN is a significant model in artificial neurology. Based on the analysis of the mathematical model of CNN, some properties of a CNN, including uniqueness and boundedness, global stability, fault tolerance, bifurcation, and chaotic characteristics, are further studied.[11–13] The activation function (output function) in the original Chua–Yang CNN is a piecewise linear function, which cannot sufficiently imitate other types of nonlinear functions. Therefore, it is necessary and meaningful to propose nonlinear dynamic CNN systems with more complex functions. The introduction of chaotic dynamics enables neuron networks to possess more complex dynamics and various attractors. The synapses and the axons are the basic computing and information processing units in the brain. As a perfect element to simulate neural synapse and axons, the memristors can be introduced into chaotic neural networks, which can not only emulate memory and learnings, but also resemble the pattern of human brain information processing mode.

By introducing memristive synaptic weight instead of resistive synaptic weight, some researches have reported the research results about the complex dynamic behaviors of memristive neural networks.[14,15] In Ref. [16] a new memristive CNN model was proposed, which proved that the memristive CNN has both short-term (volatile) storage functions and long-term (non-volatile) storage functions, and can also display the interesting two-dimensional (2D) waves. In Ref. [17],

†Corresponding author. E-mail: wanggyi@163.com

© 2022 Chinese Physical Society and IOP Publishing Ltd

a discrete memristor-based CNN was introduced, which can perform logic operations, image processing, complex behaviors, and advanced brain functions by changing the characteristics of the memristors. Very recently, in Ref. [18] it was proved that using memory-based CNNs for associative memory will greatly increase storage capacity. In Ref. [19] a new multi-layer RTD-M-CNN model was proposed, which can improve the density and resolution of multi-layer CNN circuits, thereby increasing the feasibility of implementing VLSI circuits. In Refs. [20,21], two kinds of memristive neural networks were proposed, which can exhibit complex dynamical behaviors, including self-exited quasi-periodic limit cycle, chaotic attractor, and hyperchaotic attractor. In Ref. [22], a fractional-order quaternion neural network was put forward, in which the aperiodic, chaotic, and hyperchaotic dynamical behaviors are found by numerical simulations. The memristor has become one of the best candidates for artificial neural networks.[23–26]

In Ref. [27], a novel hyperbolic-type memristor-based 3-neuron Hopfield neural network (HNN) was proposed, which is achieved through substituting one coupling-connection weight with a memristive synaptic weight. Unlike Ref. [27], the present paper introduces a new hyperbolic-tangent memristor model, based on which a new memristor-based CNN with 3-neurons[28] is constructed. We show that for different system parameters, the asymmetric coexistence behaviors of different types of attractors and the offsets of the positions of attractors can be formed under different initial conditions. Finally, the complexities of different types of attractors are analyzed and validated by Pspice circuit simulations.

2. Hyperbolic-type memristor-based CNN

2.1. Cellular neural network-CNN

The basic circuit unit of a CNN is called a cell, which consists of linear and nonlinear circuit elements. Consider an $M \times N$ CNN, which has $M \times N$ cells arranged in M rows and N columns. A 2D 3×3 CNN is shown in Fig. 1.

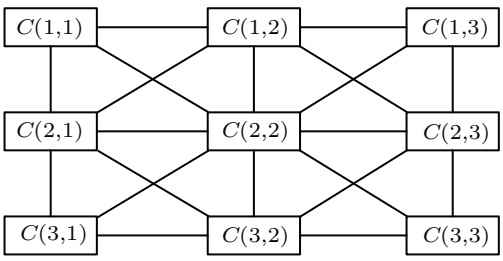


Fig. 1. 2D 3×3 CNN.

In Fig. 1, it is supposed that the cell $C(i,\ j)$ is only connected to the cells in the range of r, and $N_r(i,\ j)$ is the set of cell $C(i,\ j)$ and its neighboring cells, which is defined as

$$N_r(i,j) = \{C(k,l)\,|\max(|k-i|\,,|l-j|)|\le r\},$$
$$1 \le k \le M;\ \ 1 \le l \le N, \tag{1}$$

where r is a positive integer number. The equivalent circuit diagram of a cellular neuron, consisting of capacitance, resistances, controlled sources, and independent sources, is shown in Fig. 2, where $I_{xu}(i,j;k,l) = B(i,j;k,l)\,u_{kl}$, $I_{xy}(i,j;k,l) = A(i,j;k,l)\,y_{kl}$, where u, x, and y denote the input, state, and output, respectively.

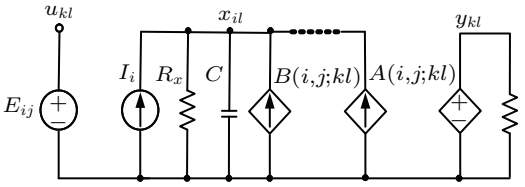


Fig. 2. Equivalent circuit of cell $C(i,\ j)$.

The state equation of cell $C(i,\ j)$ can be described by

$$C\frac{\mathrm{d}x_{ij}(t)}{\mathrm{d}t} = -\frac{1}{R_x}x_{ij}(t) + \sum_{C(k,l)\in N_r(i,j)} A(i,j;k,l)\,y_{kl}(t) + \sum_{C(k,l)\in N_r(i,j)} B(i,j;k,l)\,u_{kl}(t) + I. \tag{2}$$

And the corresponding activation function $y_{kl}(t)$ is given by

$$y_{ij}(t) = f(x_{ij}(t)) = \frac{1}{2}(|x_{ij}(t)+1| - |x_{ij}(t)-1|), \tag{3}$$

where $x_{ij}(t)$ denotes the state of cell unit $C(i,\ j)$, and $u_{kl}(t)$ is the input of $C(i,\ j)$. As an activation function, $y_{ij}(t)$ is the output, $B(i,\ j;\ k,\ l)$ and $A(i,\ j;\ k,\ l)$ are a control operator and a feedback operator, respectively, I is the input bias current, and R_x is the output impedance.

By setting $C = 1$, $R_x = 1$, and $I = 0$ in Eq. (2), a simple CNN model is described by

$$\frac{\mathrm{d}x_i(t)}{\mathrm{d}t} = -x_i(t) + \sum_{k=1}^{3} A_{ik}y_k(t) + \sum_{k=1}^{3} B_{ik}u_k(t), \quad (i = 1,2,3). \tag{4}$$

The system function can be determined by 21 parameters in A, B, and I, which are defined as follows:[29]

$$A = \begin{bmatrix} a_{11} & a_{12} & a_{13} \\ a_{21} & a_{22} & a_{23} \\ a_{31} & a_{32} & a_{33} \end{bmatrix},$$
$$B = \begin{bmatrix} b_{11} & b_{12} & b_{13} \\ b_{21} & b_{22} & b_{23} \\ b_{31} & b_{32} & a_{33} \end{bmatrix}, \quad I = \begin{bmatrix} I_1 \\ I_2 \\ I_3 \end{bmatrix}. \tag{5}$$

The activation function is an abstract concept in biology, which represents the potential discharge rate of a neuron. Normally, the neuron's discharge rate stays at zero. When an input current is received, the discharge rate starts to increase rapidly and gradually approaches to an asymptote. Mathematically,

this asymptote looks like a hyperbolic tangent function. Because the hyperbolic tangent function is smooth, it is convenient for theoretical analysis. So, we take

$$y_{kl}(t) = \tanh(x_{kl}(t)) \tag{6}$$

as an activation function.[19]

2.2. Hyperbolic-type memristor

A neuron activation function is a monotonic differentiable function which is bounded above and below. Therefore, a hyperbolic tangent function is usually utilized as the neuron activation function. For this reason, a new hyperbolic-type memristor is proposed and its constitutive relation between current and voltage is modeled as

$$\begin{aligned} \mathrm{i} &= W(w)\, v = [a - b\tanh(w)]\, v, \\ \tau \frac{\mathrm{d}w}{\mathrm{d}t} &= v - cw, \end{aligned} \tag{7}$$

where v and i represent the voltage and current of the memristor, respectively; w is the internal state variable; τ is integral time constant; a, b, and c are constants of the memristor where $c > 0$. In the case of $a < 0$, the memristor is active. When $a = -1$, $b = -6$, $c = 0.1$, and a sinusoidal voltage $v = V_m \sin(2\pi f t)$ is applied to the memristor, we can derive an instantaneous power diagram and a memductance diagram as shown in Fig. 3. Observe that when memductance $W(x) < 0$, there is always $p(t) < 0$, which corresponds to the activity of the memristor as show in Fig. 3(b).

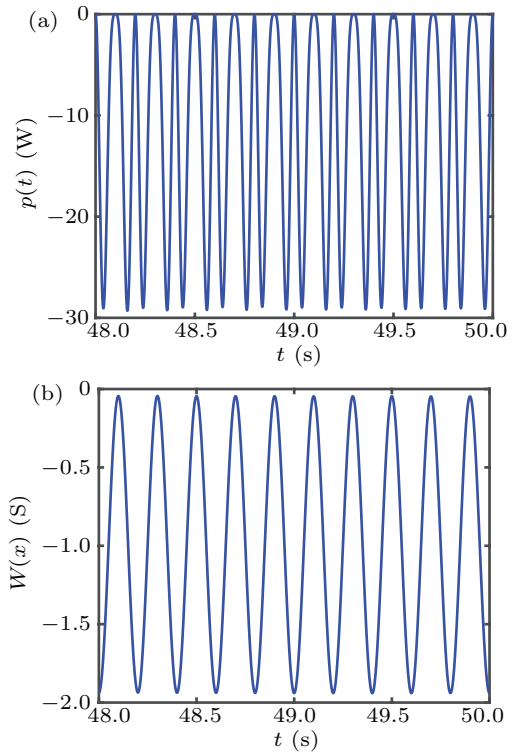


Fig. 3. (a) Instantaneous power $p(t)$ and (b) memductance $W(x)$.

When $a = -1$, $b = -6$, and $c = 0.1$, under the excitation of the sinusoidal voltage with frequency $f = 3$ Hz, 5 Hz, 10 Hz, 30 Hz, and 150 Hz, and amplitude $V_\mathrm{m} = 5$ V, 4 V, and 3 V, the frequency- and amplitude-dependent pinched hysteresis curves are plotted in Fig. 4, which shows that each lobe area decreases with the increase of the frequency while increases with the increase of the amplitude, and that the hyperbolic-type memristor can behave three essential characteristics of memristors. Since the v–i characteristic curves exist in the second and fourth quadrant, the proposed memristor is an active memristor.

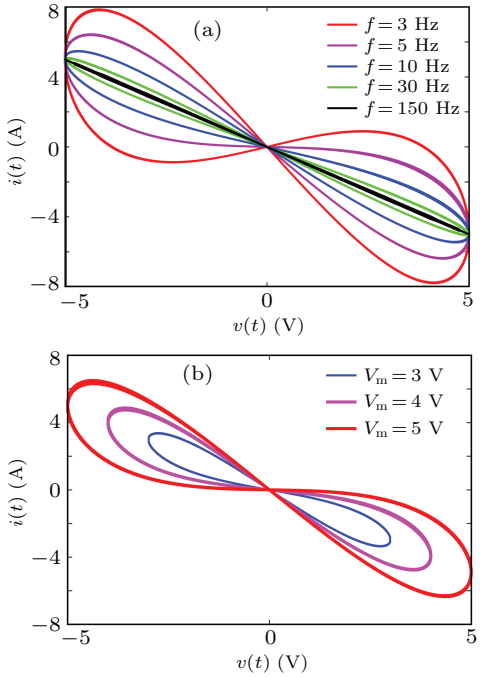


Fig. 4. Numerically simulated pinched hysteresis loops of the hyperbolic-type memristor. (a) $V_\mathrm{m} = 4$ V with different stimulus frequencies; (b) $f = 5$ Hz with different stimulus amplitudes.

The corresponding equivalent circuit of the proposed memristor is designed as shown in Fig. 5. The input voltage v is sent to the integral circuit consisting of U0 and C1 via inverting proportional amplifier U1, where the output of U0 is the state w. Through the inversing hyperbolic tangent function circuit and the inverting amplifier U2, the memductance W transforms into the multiplier, whose output is described as

$$W(w) = -\left(\frac{R_5}{R_6} v_1 - \frac{R_5}{R_4}\tanh(w)\right). \tag{8}$$

The equivalent circuit of $-\tanh$ in the solid wire box is shown in Fig. 5(b). It is easy to see that the inverting tangent hyperbolic function can be achieved by a pair of transistors T_1 and T_2, a constant current source I_0 and two controllable gain operation amplifier circuits.

When the excitation voltage is $v_1 = -1$ V, the simulated pinched hysteresis curve is shown in Fig. 6(a), where the horizontal axis represents the excitation voltage v and the vertical axis denotes the current i. The transfer characteristics of the inversing hyperbolic tangent function are shown in Fig. 6(b). The hysteresis curve of the memristor obtained by the Matlab numerical simulation is shown in Fig. 6(c).

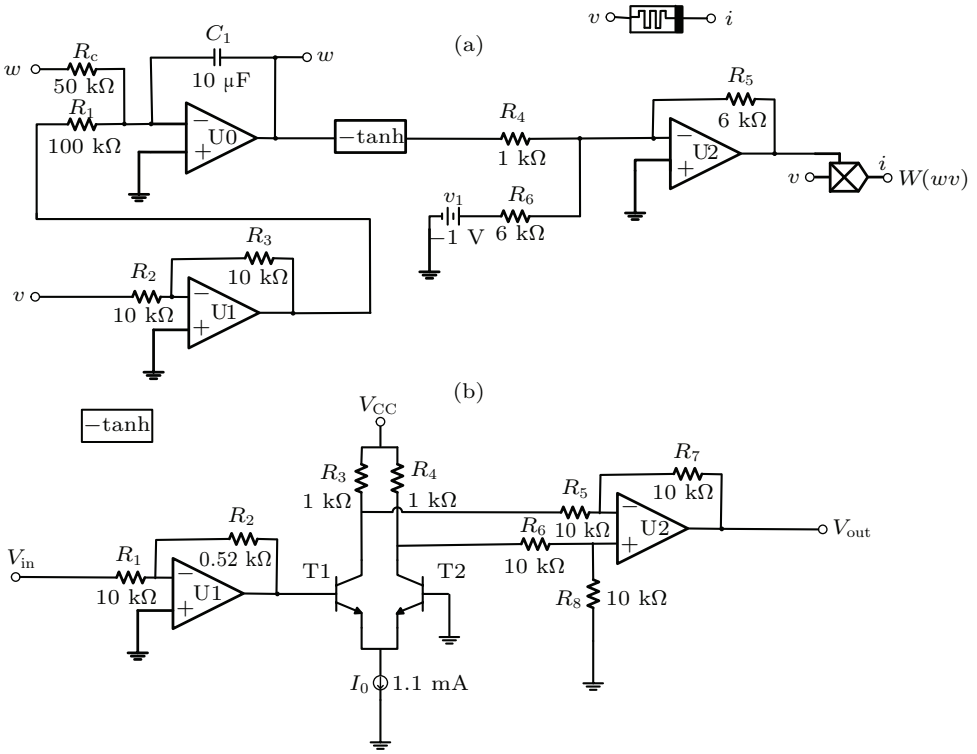


Fig. 5. Equivalent circuit of hyperbolic-type memristor characterized by Eq. (7): (a) circuit realization schematic diagram; (b) schematic diagram of the inverting tangent hyperbolic function circuit.

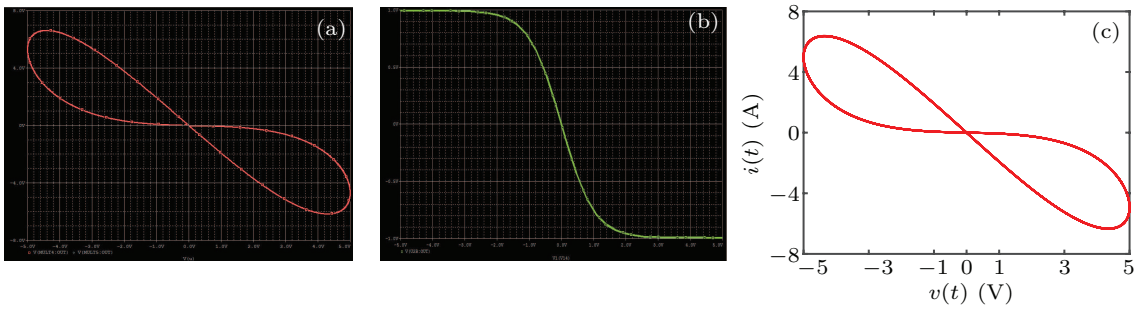


Fig. 6. (a) Hysteresis curve of memristor obtained by Pspice circuit simulation, (b) transfer characteristic of "$-\tanh(\cdot)$" block, and (c) hysteresis curve obtained by Matlab numerical simulation.

2.3. Chaotic behavior of memristor-based CNN

Now, the proposed memristor-based CNN cell is shown in Fig. 7.

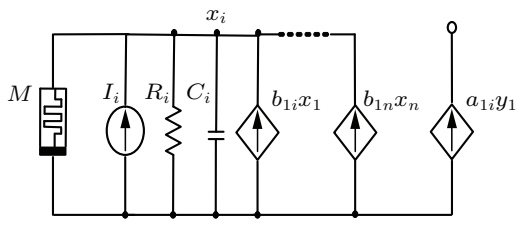


Fig. 7. Memristor-based CNN cell.

The connection matrix of the CNN consisting of three cells has the following form:

$$A=\begin{bmatrix} 3 & 0 & 5 \\ -5 & 0 & 0 \\ W & 0 & 0 \end{bmatrix},\quad B=\begin{bmatrix} -2 & 2 & d \\ 1 & 0 & 1 \\ 0 & -9 & 1 \end{bmatrix}. \tag{9}$$

The autonomous ordinary differential equations describing the proposed memristive neural network can be derived in a dimensionless form as follows:

$$\begin{cases} \dfrac{\mathrm{d}x}{\mathrm{d}t} = 3\tanh(x)+5\tanh(z)-3x+2y+dz, \\ \dfrac{\mathrm{d}y}{\mathrm{d}t} = -5\tanh(x)+x-y+z, \\ \dfrac{\mathrm{d}z}{\mathrm{d}t} = W(w)\tanh(x)-9y, \\ \dfrac{\mathrm{d}w}{\mathrm{d}t} = \tanh(x)-cw, \end{cases} \tag{10}$$

where x, y, and z represent the state variables of each cell, w is the internal state variable of the memristor, d is the system parameter, $W(w)$ is the memristance and $W(w)=a-b\tanh(w)$ denoting the synaptic weight a_{31} connecting the first and third neurons. Thus, the hyperbolic-type memristor-based CNN can be modeled by Eq. (10), which is a four-dimensional autonomous nonlinear dynamical system.

When $a=-1$, $b=-2$, $c=0.9$, $d=-3$, and the initial condition is taken as (0, 0, 0.1, 0), the system exhibits chaotic behavior, whose attractors are shown in Fig. 8.

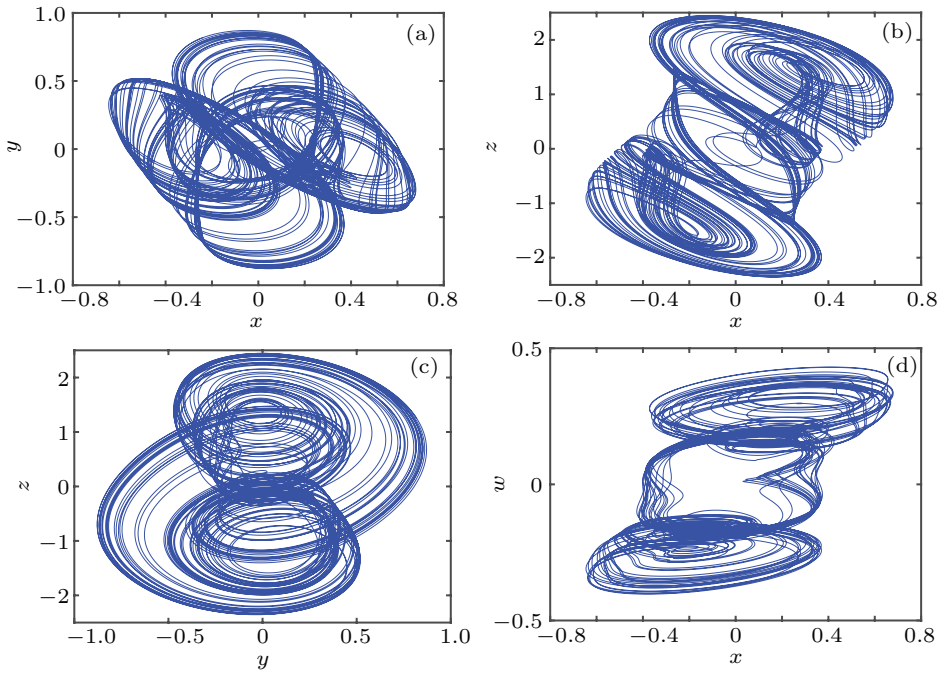


Fig. 8. Phase portraits of proposed chaotic CNN in (a) x–y plane, (b) x–z plane, (c) y–z plane, and (d) x–w plane.

Using the Jacobian method we can obtain the Lyapunov exponents of Eq. (10) as (0.4796, 0, −0.9082, −1.7535), and the corresponding Lyapunov dimension is $DL = 2.7558$. Figure 9 shows the Poincare mapping at $y = 0$ and the time domain wave-forms of x, y, and z, which is aperiodic and pseudo-random.

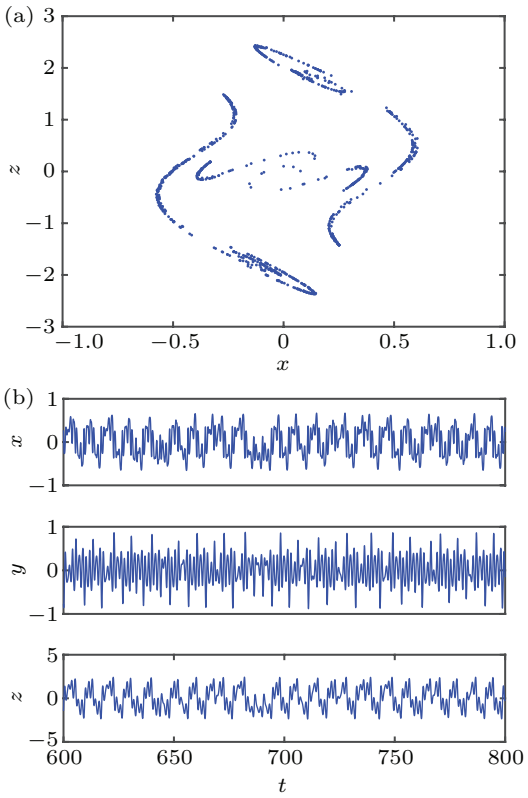


Fig. 9. (a) CNN Poincare map at $y = 0$ (projection in x–z plane), (b) CNN time domain waveform of x, y, and z components.

3. Equilibrium points and stability

By solving equations $\dot{x} = \dot{y} = \dot{z} = \dot{w} = 0$, three equilibrium points are determined as $P_0 = (0,0,0,0)$, $P_1 = (x_1, y_1, z_1, w_1)$, and $P_2 = (x_2, y_2, z_2, w_2)$, where the nonzero equilibrium points P_1 and P_2 can be calculated by solving the following equations:

$$\begin{cases} H = 3\tanh(x_i) + 5\tanh(z_i) - 3x_i + 2y_i + dz_i = 0, \\ y_i = \dfrac{a - b\tanh(w_i)}{9} \cdot \tanh(x_i), \\ z_i = y_i - x_i + 5\tanh(x_i), \\ w_i = \dfrac{\tanh(x_i)}{c}. \end{cases} \tag{11}$$

The values of x_1 and x_2 can be determined through graphic method as shown in Fig. 10. Then the values of y_i, z_i, and w_i ($i = 1, 2$) can be obtained by substituting x_1 and x_2 into Eq. (11).[17] Taking $a = -1$, $b = -2$, $c = 0.1$, and $d = -3$ for example, the function curve given in Eq. (11) is plotted in Fig. 10, from which the solutions are obtained as $x_1 = 0.3948$ and $x_2 = -0.3945$. Correspondingly, the two nonzero equilibrium points can be easily obtained from Eq. (11): $P_1 = (0.3948, 0.0416, 1.5243, 3.7549)$ and $P_2 = (-0.3945, 0.1250, -1.3567, -3.7523)$.

The Jacobian matrix at the equilibrium point $P = (\bar{x}, \bar{y}, \bar{z}, \bar{w})$ is derived from Eq. (10) as follows:

$$J = \begin{bmatrix} -3 + 3h_1 & 2 & 5h_3 + d & 0 \\ 1 - 5h_1 & -1 & 1 & 0 \\ \bar{W}h_1 & -9 & 0 & -b\tanh(\bar{x}) \cdot h_4 \\ h_1 & 0 & 0 & -c \end{bmatrix}, \tag{12}$$

where $h_1 = 1 - \tanh^2(\bar{x})$, $h_3 = 1 - \tanh^2(\bar{z})$, $h_4 = 1 - \tanh^2(\bar{w})$, and $\bar{W} = a - b\tanh(\bar{w})$.

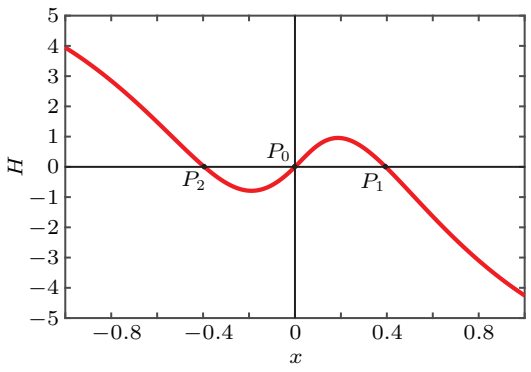


Fig. 10. Function curve and its intersections with the x axis, where $a=-1$, $b=-2$, $c=0.1$, and $d=-3$.

For the zero-equilibrium point $P_0=(0,0,0,0)$, the characteristic equation is yielded as

$$P(\lambda) = \det(E\lambda - J) = a_0\lambda^4 + a_1\lambda^3 + a_2\lambda^2 + a_3\lambda + a_4 = 0, \tag{13}$$

where

$$\begin{cases} a_0 = 1, \\ a_1 = 1+c, \\ a_2 = 17 - a(5+d) + c, \\ a_3 = 17c - ac\cdot(5+d) - (36+a)(5+d) - 2a, \\ a_4 = -(36+a)(5+d)\cdot c - 2ac. \end{cases} \tag{14}$$

According to the Routh–Hurwitz criterion, when

$$\Delta_1 = a_1 > 0, \quad \Delta_2 = \begin{vmatrix} a_1 & a_0 \\ a_3 & a_2 \end{vmatrix} > 0,$$
$$\Delta_3 = \begin{vmatrix} a_1 & a_0 & 0 \\ a_3 & a_2 & a_1 \\ a_5 & a_4 & a_3 \end{vmatrix} > 0,$$
$$\Delta_3 = \begin{vmatrix} a_1 & a_0 & 0 & 0 \\ a_3 & a_2 & a_1 & a_0 \\ a_5 & a_4 & a_3 & a_2 \\ a_7 & a_6 & a_5 & a_4 \end{vmatrix} > 0, \tag{15}$$

the real parts of the eigenvalues are negative, implying that the CNN is stable. So, if the CNN is chaotic, there should be at least one positive real part of the eigenvalue, which leads to the consequence that not all the expressions of Eq. (15) are positive.[30] For example, when $a=-1$, $b=-2$, $c=0.1$, and $d=-3$, the zero equilibrium point has $\Delta_1=1.1$, $\Delta_2=87.1$, $\Delta_3=-5749.7$, and $\Delta_4=39154$; the equilibrium point $P_1=(0.3948,0.0416,1.5243,3.7549)$ has $\Delta_1=1.5$, $\Delta_2=-41.6$, $\Delta_3=-2890.8$, and $\Delta_4=-19336.1$; and the equilibrium point $P_2=(-0.3945,0.1250,-1.3567,-3.7523)$ has $\Delta_1=1.5$, $\Delta_2=-42.3$, $\Delta_3=-2543.8$, and $\Delta_4=-14832.3$. Under this condition, all the equilibrium points are unstable, thus creating the possibility of chaos. The eigenvalues of the three equilibrium points are listed in Table 1.

Table 1. Characteristic roots of equilibrium points and their stability where $a=-1$, $b=-2$, $c=0.1$, and $d=-3$.

Equilibrium points	λ_1	λ_2	λ_3	λ_4	Stability
P	−0.1	2.468	−1.73381 + 4.95487i	−1.73381–4.95487i	instability point
P_1	−2.987	−0.1	0.78205 + 4.68014i	0.78205–4.68014i	instability point
P_2	−3.326	−0.1	0.95192 + 4.08877i	0.95192–4.08877i	instability point

4. Dynamic behavior of the system

4.1. Bifurcation with parameter *d*

As the system parameters change, the system can exhibit various dynamical behaviors. Let $a=-1$, $b=-2$, and $c=0.9$, the bifurcation diagram and the corresponding Lyapunov exponents with respect to parameter d over the range $-4<d<5$ are shown in Fig. 11, where the initial conditions are (0, 0, 0.1, 0). From the figure it can be seen that with the parameter d increasing gradually, the system state changes between the limit cycle and chaos. Figure 12 shows six different attractors.

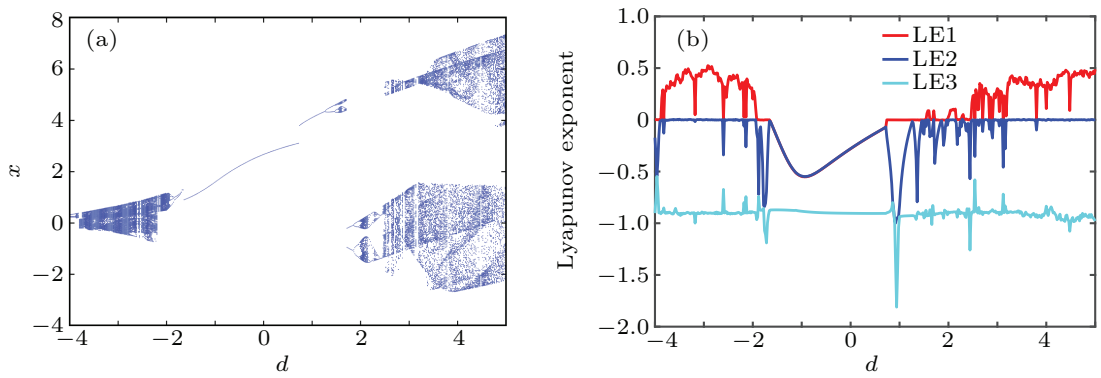


Fig. 11. (a) Bifurcation and (b) Lyapunov exponent (LE) with respect to d.

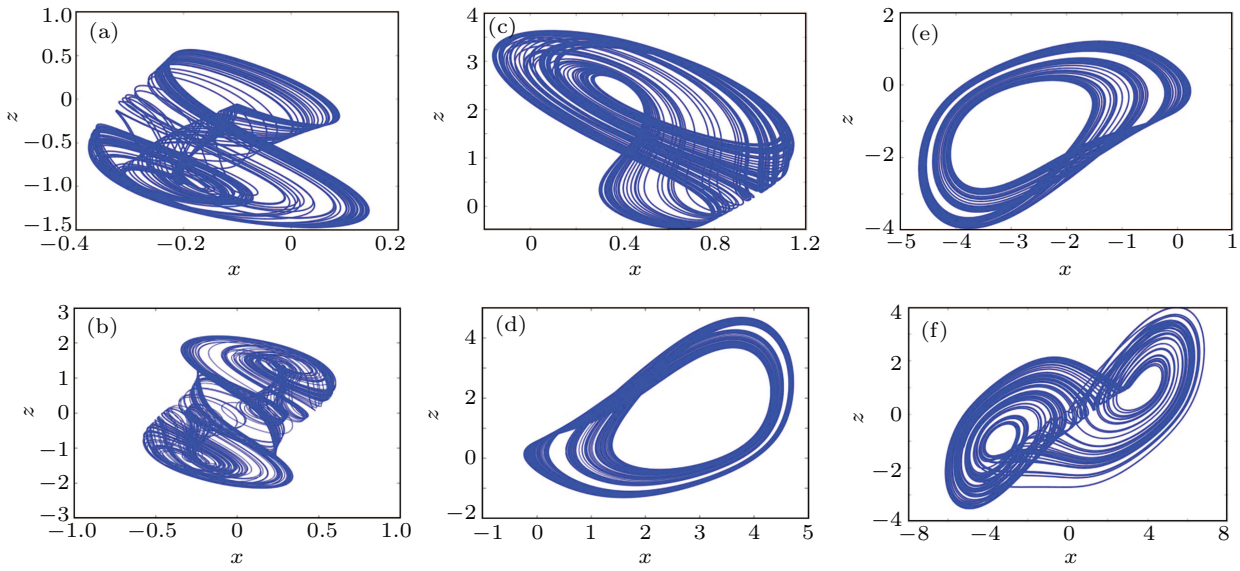


Fig. 12. Projections on w–y phase plane of attractors observed for $d = -3.8$ (a), -3.2 (b), -2 (c), 1.6 (d), 2.1 (e), and 4.2 (f).

4.2. Asymmetric coexisting attractors varying with parameter *b*

Coexisting attractors refer to different types of attractors in a nonlinear system when the initial values change but the system parameters remain unchanged. Now, we investigate the bifurcations of the system with respect to both initial values and system parameters, where the initial conditions are selected as (0, 0, 0.1, 0), (0, 0, -0.1, 0), and (0.5, 0, 0, 1), and the parameter d is set to be -4, -2.5, and 3. For each fixed parameter d, the coexisting behaviors of the memristor-based CNN can be revealed by the bifurcation diagrams with both parameter b and the initial conditions.

4.2.1. Case 1 for $d = -4$

When $a = -1$, $c = 0.1$, and $d = -4$, the bifurcation diagrams of state variable x and the corresponding first three Lyapunov exponents with respect to both parameter b and the three initial conditions over the range $-10 < b < 0$ are shown in Fig. 13, in which the red, blue, and black bifurcations correspond to the initial conditions (0, 0, 0.1, 0), (0, 0, -0.1, 0), and (0.5, 0, 0, 1), respectively, and the corresponding Lyapunov exponents are shown in Figs. 13(b) and 13(d).

Figure 13 shows that there are three different bifurcation diagrams, which correspond to the three different conditions and multiple coexisting attractors, including stable point attractor, periodic and chaotic attractors, as shown in Fig. 14.

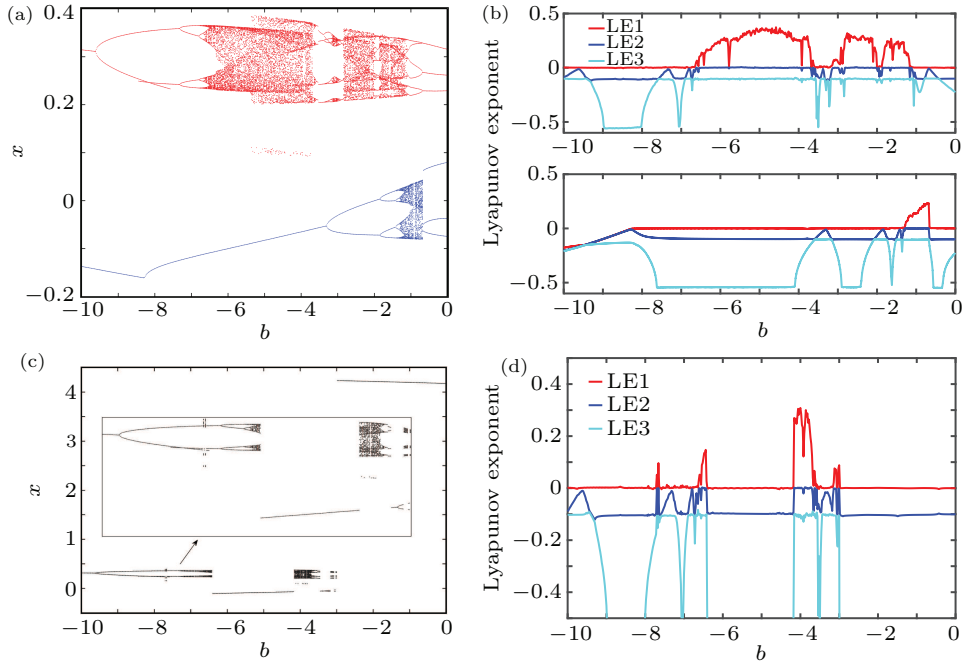


Fig. 13. Coexisting behaviors of asymmetric attractors with b increasing, where $a = -1$, $c = 0.1$, and $d = -4$. ((a), (c)) Bifurcation diagrams of the state variable x, with red, blue, and black orbits corresponding to initial values (0, 0, 0.1, 0), (0, 0, –0.1, 0), and (0.5, 0, 0, 1); ((b), (d)).

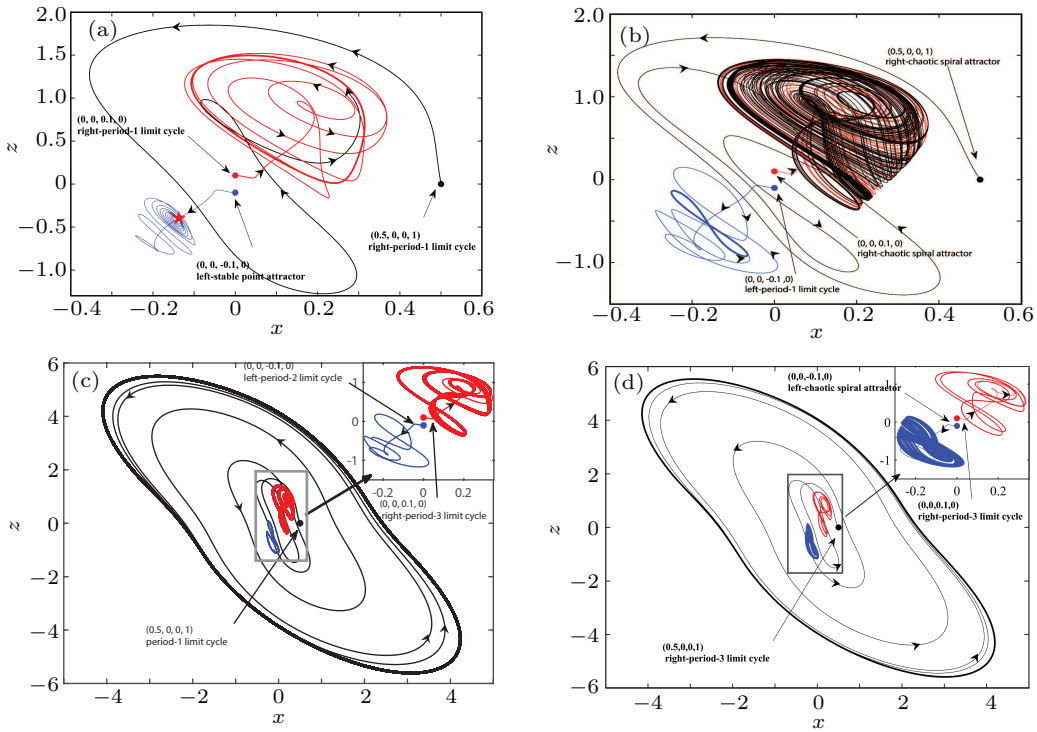


Fig. 14. Phase portraits of asymmetrical coexisting attractors with different initial conditions and different values of parameter b in x–z plane. (a) Coexistence of left-stable point attractor (marked with five-pointed star) and right-period-1 limit cycle (red) at $b = -10$; (b) coexistence of left-period-1 limit cycle (blue) and right-chaotic spiral attractors at $b = -4$; (c) coexistence of period-1 limit cycle, left-period-2 limit cycle, and right-period-3 limit cycle at $b = -2$; (d) coexistence of period-1 limit cycle, left-chaotic spiral attractor, and right-period-3 limit cycle at $b = -1$.

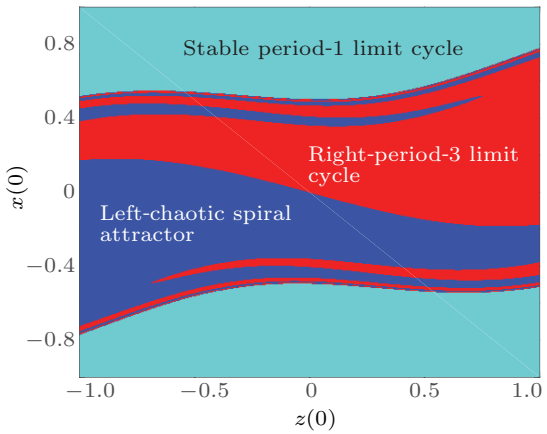


Fig. 15. Basin of attraction with $x(0)$ and $z(0)$.

It follows that the dynamic behavior depends on initial conditions of the system, which reflects the sensitive dependence of the system state on the initial conditions. Figure 15 describes the basin of attraction with respect to initial conditions $x(0)$ and $z(0)$, where the red regions indicate the right-period-3 limit cycles, the blue regions refer to the left-chaotic spiral attractors, and the sky blue regions represent the period-1 limit cycles.

4.2.2. Case 2 for $d = -2.5$

When $a = -1$, $c = 0.1$ and $d = -2.5$, the bifurcation diagrams and the corresponding Lyapunov spectrums *versus* parameter b for the initial conditions (0, 0, 0.1, 0) (red bifurcation diagram) and (0, 0, −0.1, 0) (blue bifurcation diagram) are shown in Fig. 16, in which double-scroll chaotic attractors, periodic limit cycles and other dynamic behaviors can be observed as shown in Fig. 17.

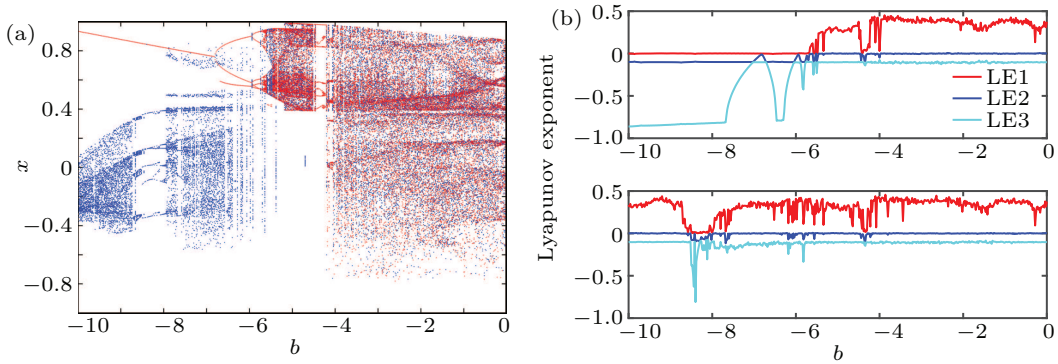


Fig. 16. Coexisting bifurcation with respect to parameter b, where $a = -1$, $c = 0.1$, $d = -2.5$. (a) Bifurcation diagrams of state variable x with respect to initial congditions (0, 0, 0.1, 0) (red), and (0, 0, −0.1, 0) (blue); (b) Lyapunov exponent spectra under the two different initial conditions.

Figure 17(a) shows the multiple coexisting attractors with the initial conditions (0, 0, −0.1, 0) and (0, 0, 0.1, 0) for $b = -9$, $b = -7.7$, $b = -6.7$, and $b = -5.54$, including the existence of a chaotic attractor and a limit cycle, and the existence of two limit cycles.

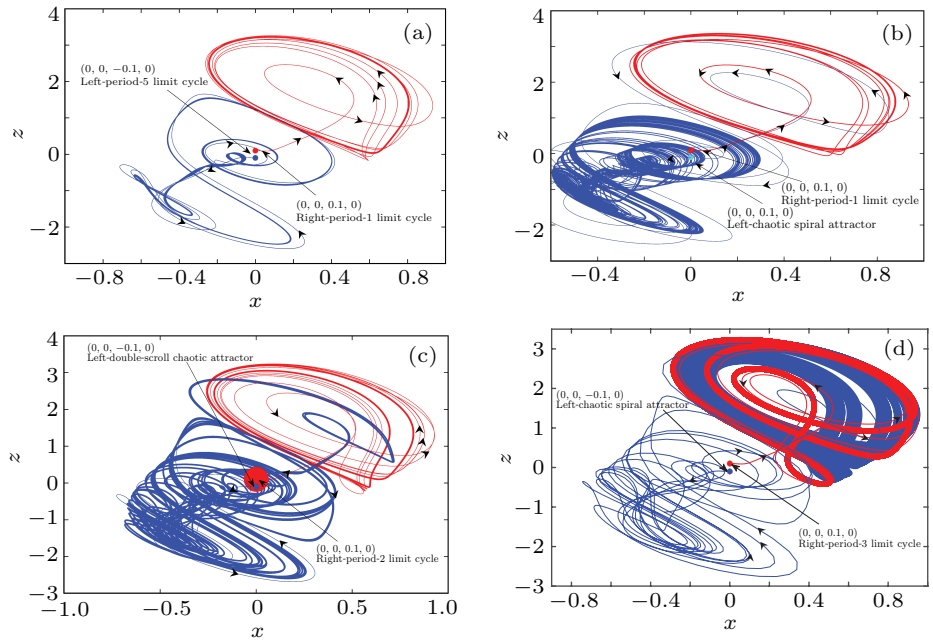


Fig. 17. Coexisting attractors with two initial conditions (0, 0, −0.1, 0) and (0, 0, 0.1, 0) for different values of parameter b in x–z plane. (a) Coexistence of two limit cycles at $b = -9$; (b) coexistence of left-period-5 chaotic attrator and right-period-1 limit cycle at $b = -7.7$; (c) coexistence of left-double-scroll chaotic attractor and right-period-2 limit cycle at $b = -6.7$; (d) coexistence of left-chaotic spiral attractor and right-period-3 limit cycle at $b = -5.54$.

Figure 18 displays the basin of attraction with respect to initial conditions $x(0)$ and $z(0)$ under the parameters $a = -1$, $b = -6.7$, $c = 0.1$, and $d = -2.5$, where the red regions indicate the chaotic spiral attractor, the blue regions represent the double-scroll chaotic attractor, and the sky blue regions refer to the period-1 limit cycle.

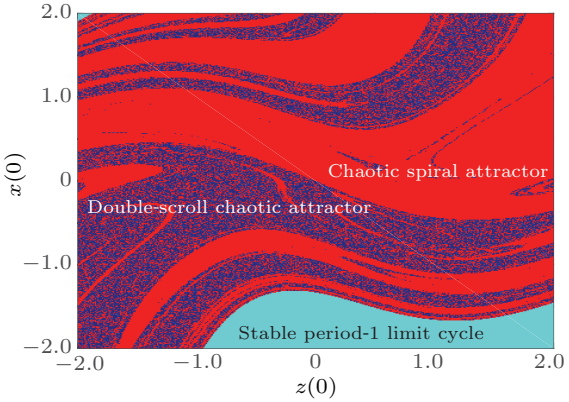


Fig. 18. Basin of attraction *versus* initial conditions $x(0)$ and $z(0)$.

4.2.3. Case 3 for $d = 3$

When $a = -1$, $c = 0.1$, and $d = 3$, the bifurcation diagrams of the state variable x and the corresponding Lyapunov exponent spectrums *versus* parameter b for different initial conditions are shown in Fig. 19, where chaotic attractors, periodic limit cycles and other dynamic behaviors can be observed. The red and blue bifurcation diagrams correspond to initial conditions (0, 0, 0.1, 0) and (0, 0, −0.1, 0), respectively, showing a coexisting bifurcation phenomenon.

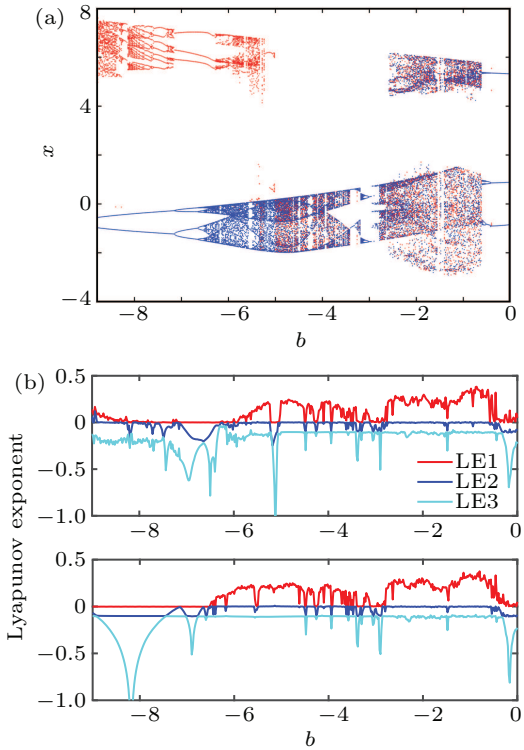


Fig. 19. Coexisting behaviors of asymmetric attractors with b increasing, where $a = -1$, $c = 0.1$, and $d = 3$. (a) Bifurcation diagram of the state variable x, where the red and blue orbits correspond to initial conditions (0, 0, 0.1, 0) and (0, 0, −0.1, 0), respectively; (b) Lyapunov exponent spectra with the two initial conditions.

Figure 20 shows several typical coexisting attractors, including coexisting period-2 limit cycle and double-scroll chaotic attractor as shown in Fig. 20(a), coexisting period-4 limit cycle and period-3 limit cycle as shown in Fig. 20(b), and coexisting spiral chaotic attractor and double-scroll chaotic attractor as shown in Figs. 20(c) and 20(d).

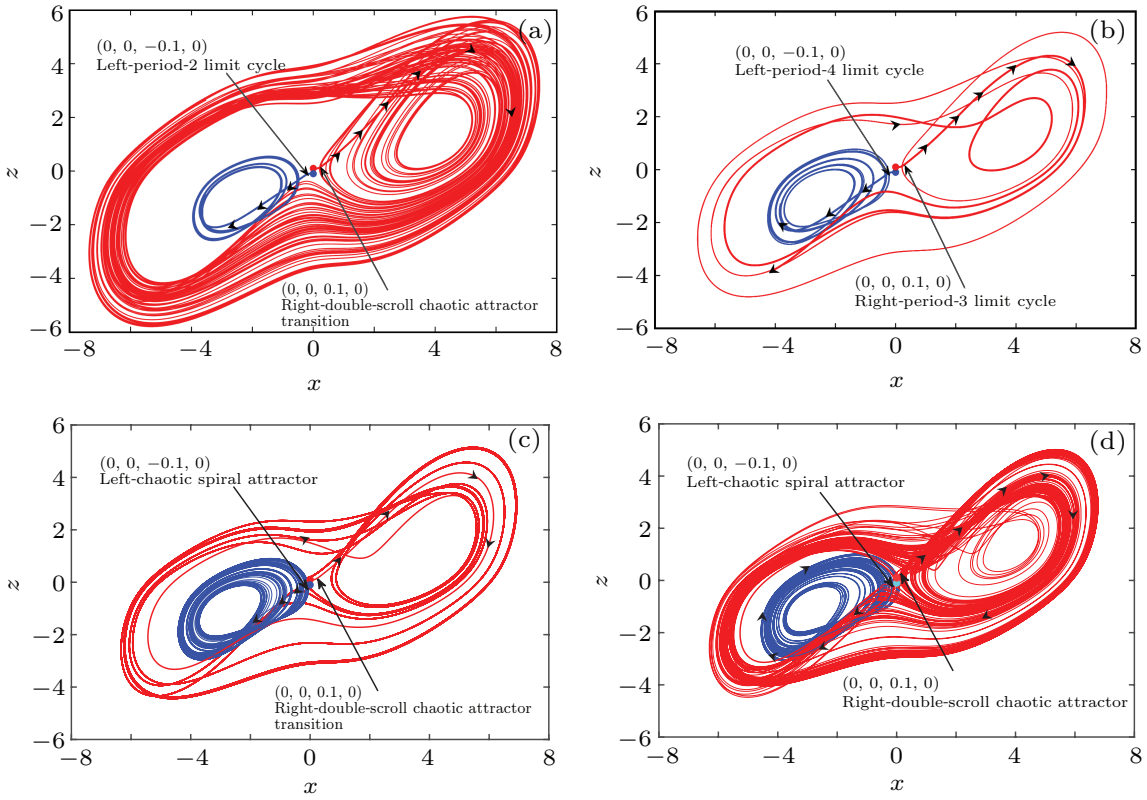


Fig. 20. Phase portraits of asymmetrically coexisting attractors with different values of b in x–z plane. (a) Coexistence of left-period-2 limit cycle and right-double-scroll chaotic attractor transition for $b = -8.5$; (b) coexistence of left-period-4 limit cycle and right-period-3 limit cycle for $b = -7$; (c) coexistence of left-chaotic spiral attractor and right-double-scroll chaotic attractor transition for $b = -6.1$; (d) coexistence of left-chaotic spiral attractor and right-double-scroll chaotic attractor for $b = -5.4$.

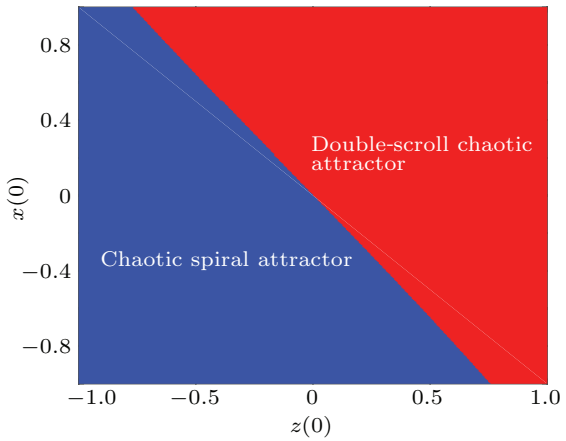


Fig. 21. Basin of attraction with respect to $x(0)$ and $z(0$.

Figure 21 shows the basin of attraction of the system with respect to the initial values $x(0)$ and $z(0)$ under the fixed parameters: $a = -1$, $b = -6$, $c = 0.1$, $d = 3$, where the red (resp. blue) region describes the case that the trajectories starting from the region eventually evolve into a double-scroll attractor (a spiral attractor). It can be seen from Fig. 21 that for the two types of attractors, the attraction domain of each one occupies half of the area of the attractor basin.

4.3. Influence of parameter c on position of the attractor

4.3.1. Case 1 for $d = -3.8$

By setting $a = -1$, $b = -2$, and $d = -3.8$, we can obtain the bifurcation diagram and the corresponding Lyapunov spectrum with respect to parameter c as shown in Fig. 22. It can be observed that with the change of parameter c, the amplitude of w changes but the Lyapunov exponents of the system are basically unchanged, so we call parameter c the chaotic amplitude modulation coefficient.[31]

It is observed from Fig. 22(a) that the amplitude of variable w approaches to zero with the increase of parameter c, which corresponds to the attractor migrating in the x–w plane plotted in Fig. 23(a), where the points with different colors represent the equilibrium points of the system corresponding to the same color attractors. It can also be seen that the attractor positions are caused to migrate by the change of parameter c, which changes the position of the corresponding the equilibrium point of the system. Several attractors are selected to show the bifurcation process in Fig. 23(b).

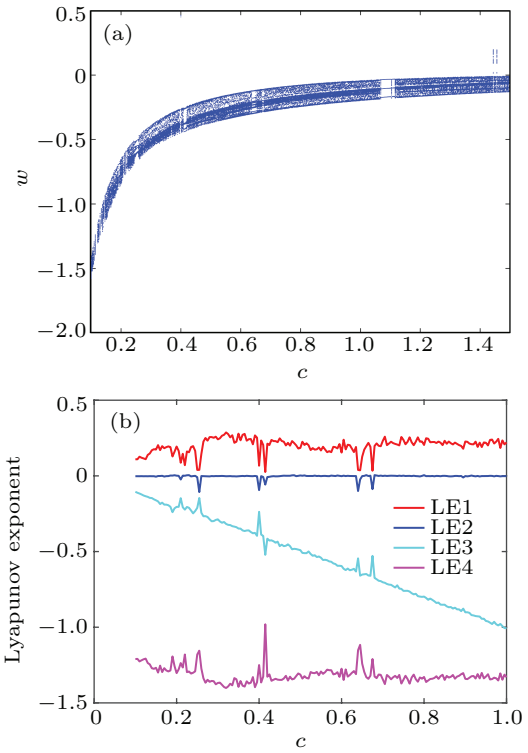


Fig. 22. (a) Bifurcation diagram and (b) Lyapunov spectrum with respect to c.

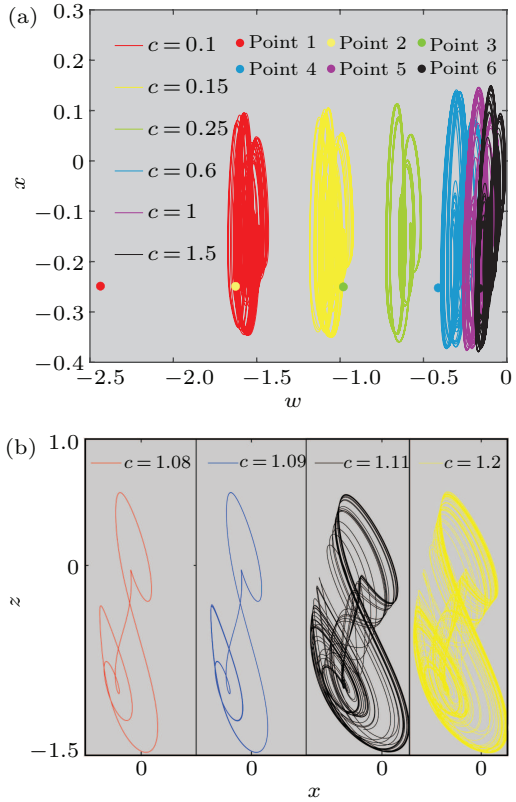


Fig. 23. Migration of attractors with the increase of c, where $a = -1$, $b = -2$, and $d = -3.8$. (a) Phase portraits of the attractors in x–w plane, and (b) bifurcation process of the attractor.

4.3.2. Case 2 for $d = 2.5$

By fixing the parameters: $a = -1$, $b = -2$, and $d = 2.5$, the bifurcation diagram of variable w and the Lyapunov exponent spectrum with respect to parameter c over the range $0.1 < c < 2$ are described in Fig. 24, from which we also observe the chaotic amplitude modulation phenomenon and the bifurcation with parameter c as shown in Figs. 24(a) and 24(b), respectively.

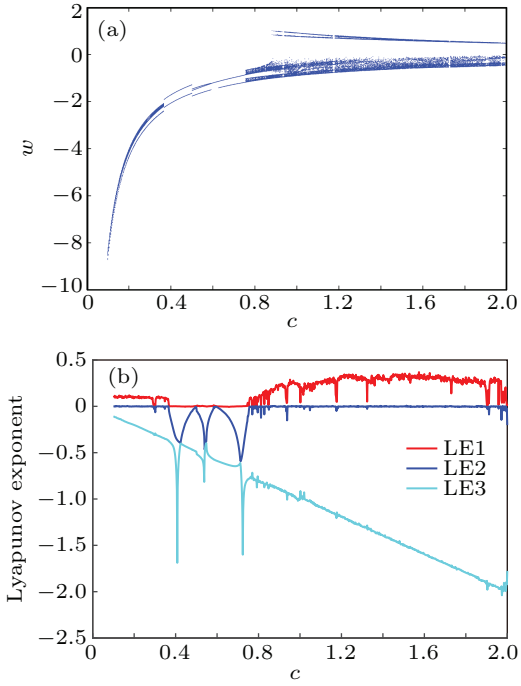


Fig. 24. (a) Bifurcation diagram and (b) Lyapunov spectrum with respect to c.

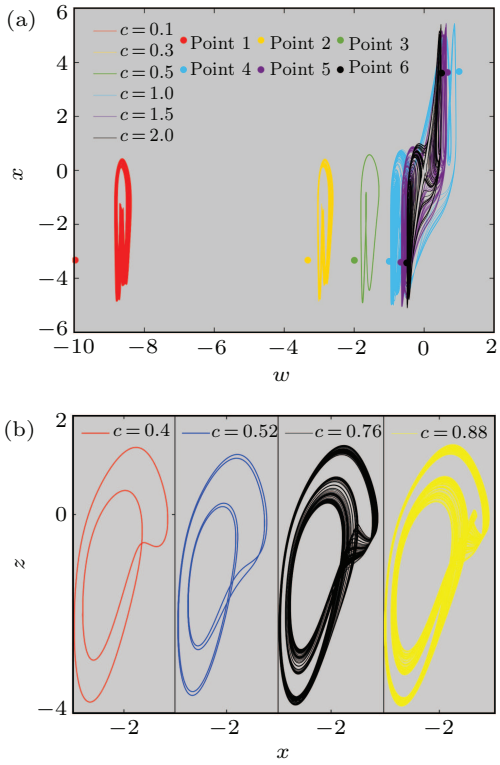


Fig. 25. Migration of attractor with c increasing, where $a = -1$, $b = -2$, and $d = 2.5$. (a) The phase portraits of attractors in x–w plane, and (b) bifurcation process of attractor.

In particular, when the parameter $c \geq 1$, the chaotic attractor evolves from a single scroll into a double scroll. Sev-

eral attractors are selected to show the bifurcation process as depicted in Fig. 25(b).

5. Complexity analysis of system

In the *SE* algorithm the energy distribution in the Fourier transform domain is used to obtain the spectral entropy based on the Shannon entropy algorithm, which can directly reflect the complexity of chaotic pseudo-random sequences.[28] The algorithm is as follows.

(i) For the reason that the spectrum can more accurately to show the signal capacity, the direct current (DC) part of the pseudo-random sequence of length N can be removed by

$$x(n) = x(n) - \tilde{x}, \tag{16}$$

where $\tilde{x} = \frac{1}{N}\sum_{n=0}^{N-1} x(n)$.

(ii) By applying the discrete Fourier transform to Eq. (16), we obtain

$$X(k) = \sum_{n=0}^{N-1} x(n) \exp\left(-\mathrm{j}\frac{2\pi}{N}nk\right) = \sum_{n=0}^{N-1} x(n) W_N^{nk}, \tag{17}$$

where $k = 0, 1, 2, \ldots, N-1$.

(iii) Taking the first half of sequence $X(k)$ and using the Parseval algorithm, we obtain the power spectrum at a specific frequency

$$p(k) = \frac{1}{N}|X(k)|^2, \tag{18}$$

where $k = 0, 1, 2, \ldots, (N/2)-1$.

The total power of the sequence can be defined as

$$p_{\mathrm{tot}} = \frac{1}{N}\sum_{k=0}^{N/2-1} |X(k)|^2, \tag{19}$$

and the probability of the relative power spectrum can be expressed as

$$P_k = \frac{p(k)}{p_{\mathrm{tot}}} = \frac{\frac{1}{N}|X(k)|^2}{\frac{1}{N}\sum_{k=0}^{N/2-1}|X(k)|^2} = \frac{|X(k)|^2}{\sum_{k=0}^{N/2-1}|X(k)|^2}, \tag{20}$$

where $\sum_{k=0}^{N/2-1} P_k = 1$.

(iv) By using Eqs. (18)–(20), and combining with Shannon entropy concept, the spectral entropy *se* of the signal is obtained from[32]

$$se = -\sum_{k=0}^{N/2-1} P_k \ln P_k. \tag{21}$$

If P_k is zero in Eq. (21), then $P_k \ln P_k$ is defined as zero. The spectral entropy converges to $\ln(N/2)$. For comparative analysis, the spectral entropy can be normalized as

$$SE(N) = \frac{se}{\ln(N/2)}. \tag{22}$$

It can be observed from the above transformation that the more unstable the power spectrum variation, the simpler the structure composition is and the less obvious the sequence amplitude. Correspondingly, the measurements are also small.

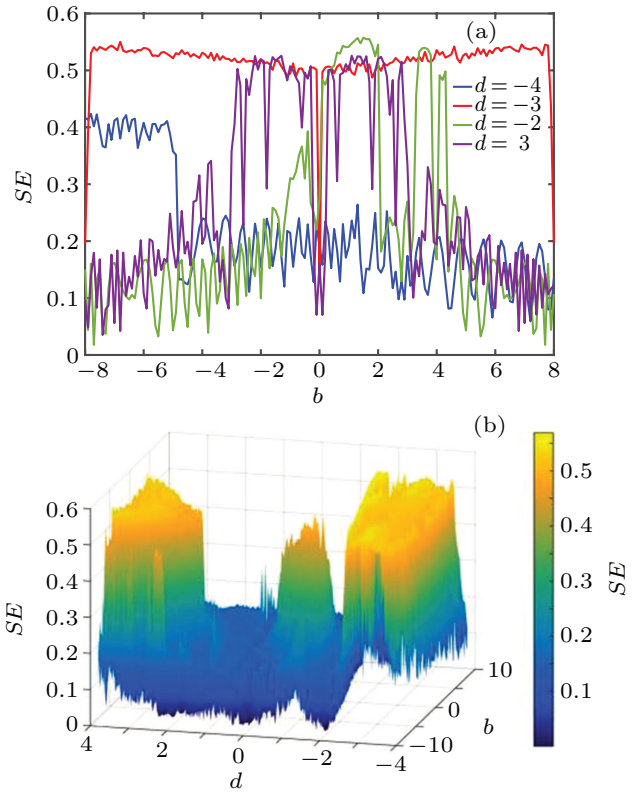


Fig. 26. (a) Two-dimensional and (b) three-dimensional *SE* curve varying with parameters b and d.

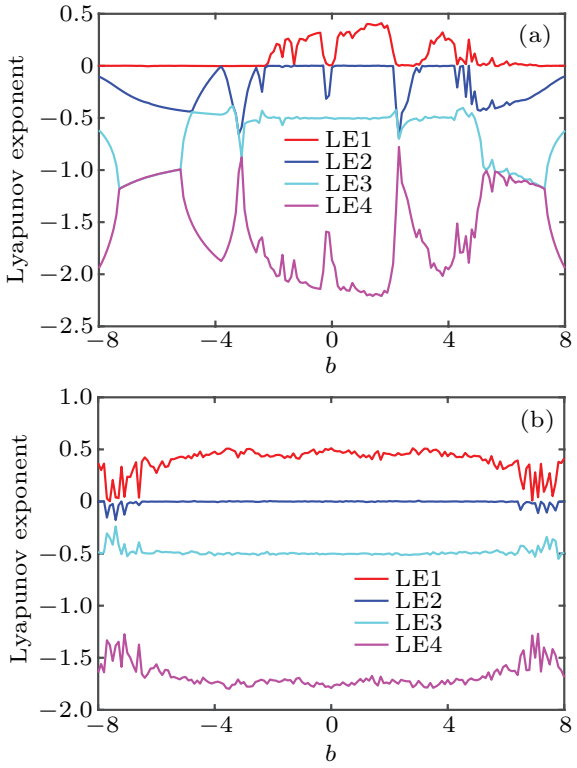


Fig. 27. Lyapunov spectrum for (a) $a = -1$, $c = 0.5$, and $d = -2$, and (b) $a = -1$, $c = 0.5$, and $d = -3$.

By fixing $a = -1$ and $c = 0.5$ and changing parameters b and d, we can calculate the complexity of memristor-based CNN system through the *SE* analysis. The two-dimensional curves and three-dimensional curves of *SE* with parameters b and d are shown in Fig. 26. For comparison, we draw the Lyapunov exponent diagram of the system for $d = -2$ and $d = -3$ as shown in Fig. 27. By comparing *SE* curve with the Lyapunov exponents, it can be seen that the complexity curve is consistent with the Lyapunov exponent spectrum, i.e., when the system is in the chaotic state, its *SE* complexity is higher, while when the system is in the periodic state, its *SE* complexity is lower. Moreover, the complexity associated with the chaotic double-scroll attractor is greater than that associated with the chaotic single-scroll attractor.

6. Simulation experiment

The Pspice circuit diagram is shown in Fig. 28 to verify the dynamic characteristics of the system.

The circuit parameters of the resistances and the capacitances are marked as shown in Fig. 28, where the internal parameters of the memristor are fixed. The x–z phase portraits of the circuit in Pspice simulations are shown in Figs. 29(a)–29(c) when the values of resistance $R_{\rm d}$ are 2.63 kΩ, 3.12 kΩ, and 5 kΩ, respectively. And the x–z phase portraits of the system simulation circuit is shown in Figs. 29(d)–29(f) when the values of resistance $R_{\rm d}$ are 6.25 kΩ, 4.76 kΩ, and 2.38 kΩ, respectively. The experimental results are shown to be in good agreement with the numerical simulation results.

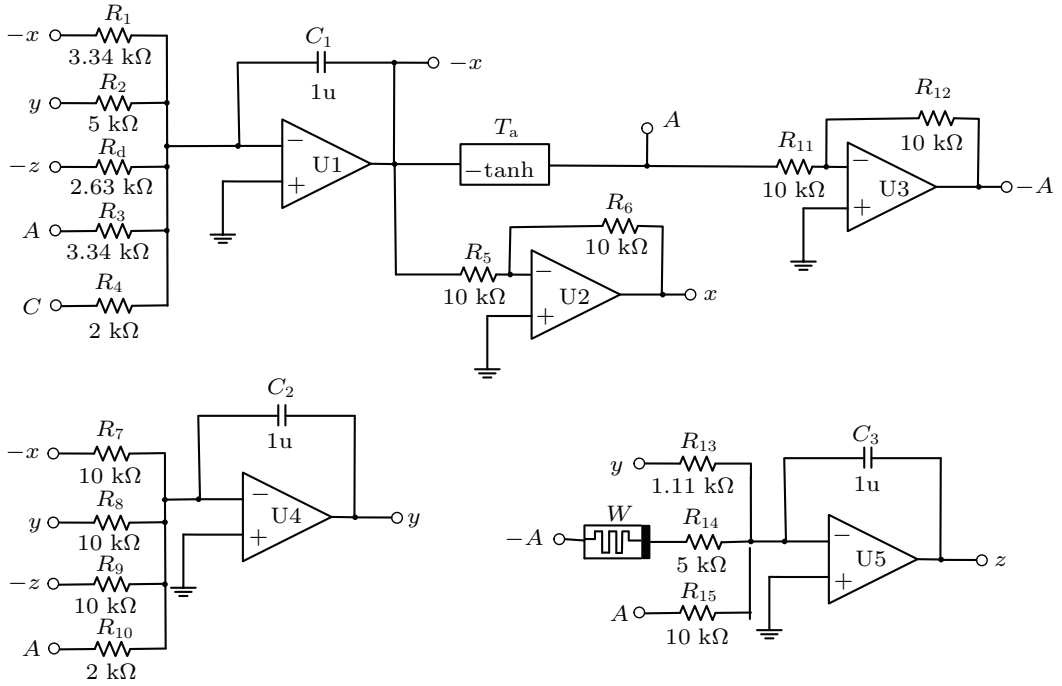


Fig. 28. Circuit realization scheme of hyperbolic-type memristor based CNN.

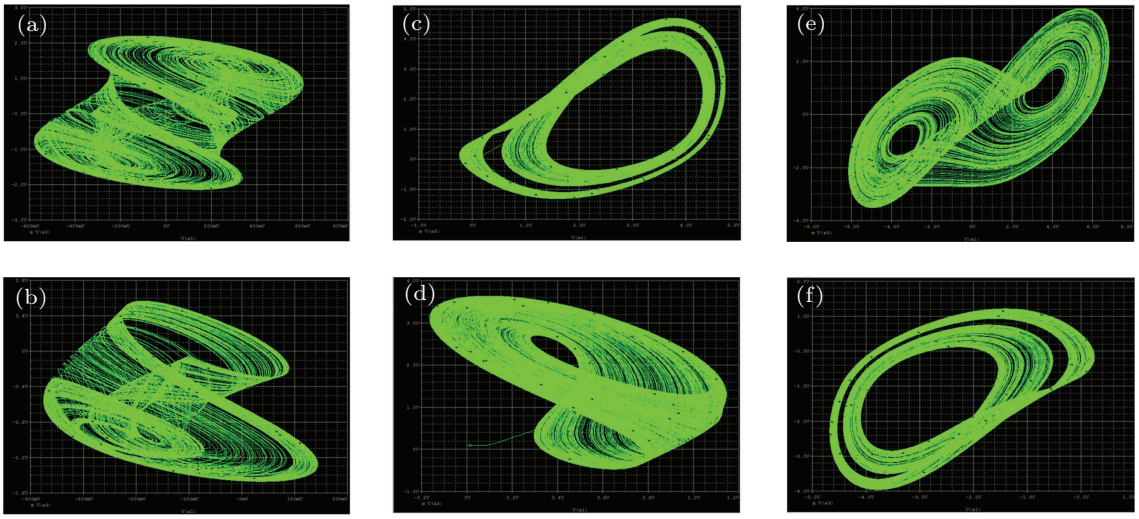


Fig. 29. Phase portraits of chaotic attractor observed from Pspice circuit simulations for (a) $R_{\rm d} = 2.63$ kΩ, (b) 3.12 kΩ, (c) 5 kΩ, (d) 6.25 kΩ, (e) 4.76 kΩ, and (f) 2.38 kΩ.

7. Conclusions

In this paper, a new hyperbolic-type memristor model is proposed. Its basic characteristics and state-dependent pinched hysteresis loops are verified by numerical simulations and theoretical analysis. A hyperbolic-type memristor-based CNN with 3 neurons is thereby constructed for generating complex chaotic behaviors in the CNN. It is found that the memristive CNN can show complex chaotic dynamics under the activation function $\tanh(\cdot)$, including state-dependent bifurcations, coexisting attractors, chaotic amplitude modulation, etc. The proposed memristor model and the memristive CNN are tested by numerical simulations and the Pspice circuit experiments.

Acknowledgement

Project supported by the National Natural Science Foundation of China (Grant Nos. 61771176 and 62171173).

References

[1] Chua L 1971 *IEEE Trans. Circuit Theory* **18** 507
[2] Strukov D B, Snider G S, Stewart D R and Stanley Williams R 2008 *Nature* **453** 80
[3] Chen L, He Z L, Li C D and Umar H G A 2019 *Advances in Difference Equations* **132**
[4] Chen L, He, Z, Li C, Wen S and Chen Y 2020 *Int. J. Bifur. Chaos* **30** 2050172
[5] Chua L and Yang L 1998 *IEEE Trans. Circ. Syst.* **35** 1257
[6] Chua L and Yang L 1998 *IEEE Trans. Circ. Syst.* **35** 1273
[7] Vaidyanathan S 2015 *International Journal of PharmTech Research* **8** 632
[8] Hu G, Rong J and Kou W 2018 *Journal of Digital Information Management* **16** 246
[9] Karakaya B, Celik V and Gulten A 2017 *Int. J. Circ. Theory Appl.* **45** 1885
[10] Korn H and Faure P 2003 *C. R. Biologies* **326** 787
[11] Chua L and Roska T 2003 *Int. J. Bifur. Chaos* **13** 1
[12] Chen A and Yuan S 2001 *Journal of Chenzhou Teachers College* **22** 6
[13] Arena P, Baglio S, Fortuna L and Manganaro M 1995 *IEEE Trans. Circ. Syst. I: Fundamental Theory and Applications* **42** 123
[14] Chen L, Li C and Chen Y 2018 *Int. J. Bifur. Chaos* **28** 1850080
[15] Chen L, Li C D, Huang T W, Hu X F and Chen Y R 2016 *Neurocomputing* **171** 1637
[16] Itoh M 2019 *Neural and Evolutionary Computing*
[17] Itoh M and Chua L 2009 *Int. J. Bifur. Chaos* **19** 3605
[18] Ahn B H, Lee J, Lin J M, Cheng H P, Hou J L and Esmaeilzadeh H 2020 arXiv: 2003. 02369v1 [cs. DC]
[19] Hu X, Feng G, Duan S and Liu L 2015 *Neurocomputing* **162** 150
[20] Li Q, Tang S and Zeng H 2014 *Nonlinear Dyn.* **78** 1087
[21] Pham V T and Jafari S 2016 *Science China Technological Sciences* **59** 358
[22] Huang X, Zhao Z and Wang Z 2012 *Neurocomputing* **94** 13
[23] Hu X F, Wang W H, Sun B, Wang Y C, Li J and Zhou G D 2021 *J. Phys. Chem. Lett.* **12** 5377
[24] Liu H J, Chen C L, Zhu X, *et al.* 2020 *Chin. Phys. B* **29** 028502
[25] Xue W H, Ci W J, Xu X H, *et al.* 2020 *Chin. Phys. B* **29** 048401
[26] Shao N, Zhang S B and Shao S Y 2019 *Acta Phys. Sin.* **68** 198502 (in Chinese)
[27] Bao B C, Qian H and Xu Q 2017 *Frontiers in Computational Neuroscience* **23** 00081
[28] Buscarino A and Fortuna L 2011 *International Symposium on Signals, IEEE*
[29] Liao L Y and Zhang X 2017 *Journal of Computational and Nonlinear Dynamics* **12** 031002
[30] Yuan F, Wang G Y and Wang X Y 2015 *Chin. Phys. B* **24** 060506
[31] Li C B, Sprott J C, Julien and Xing H Y 2016 *Int. J. Bifur. Chaos* **26** 1650233
[32] Staniczenko P P A, Lee C F and Jones N S 2009 *Phys. Rev. E* **79** 011915